Journal of the mechanical behavior of biomedical materials xxx (xxxx) xxx–xxx

Contents lists available at ScienceDirect

Journal of the Mechanical Behavior of Biomedical Materials

journal homepage: www.elsevier.com/locate/jmbbm

Open-cellular metal implant design and fabrication for biomechanical compatibility with bone using electron beam melting☆

L.E. Murr[a,b,*]

[a] Department of Metallurgical, Materials and Biomedical Engineering, The University of Texas at El Paso, El Paso, TX 79968 USA
[b] W.M. Keck Center for 3D Innovation, The University of Texas at El Paso, El Paso, TX 79968 USA

ARTICLE INFO

Keywords:
Open-cellular metal implants
Biomechanical compatibility
Electron beam melting

ABSTRACT

Implant history extends more than 4000 years in antiquity, with biocompatible alloy implants extending over only 70 years. Over the past several decades, total hip and knee replacements of Ti-6Al-4V and Co-Cr-Mo alloys have exhibited post implantation life spans extending over 15 years; limited by infection, loosening, stress-shielding-related bone resorption and other mechanical failures. With the advent of additive manufacturing technologies, such as electron beam melting (EBM) over the past decade, personalized, patient-specific; porous (open-cellular) implant components can be manufactured, and the integration of chemical, biological and mechanical methods is able to optimize strategies for improving long-term clinical outcomes. This review outlines these strategies, which include enhanced osseointegration and vascularization prospects, and provides some evidence for, and examples of, clinical trials representative of millions of implant surgeries world-wide.

1. Introduction and historical perspective

Some of the earliest implants involved carved bamboo pegs to replace missing teeth in China around 2000 BCE while similar dental pegs fabricated from copper were observed in Egyptian remains around 1000 BCE. More than 2000 years ago other cultures, including European, Asian and Mayan, were observed to use iron and gold pins to anchor decorative teeth which included shaped, carved irony, bone, sea shells, and stones; while more recent observations include both animal (heteroplastic) and human (homoplastic) tooth implants (Pal, 2015). Other early implants included hip joint components carved from ivory, pumice or plaster-of-Paris circa 1890 (Walker, 1978), although some attempts at hip arthroplasty date to the 1700s (Gomez and Morcuende, 2005). Metal implants such as plates and screws to repair bone fractures only became possible after the discovery of antiseptics and the development of X-radiology around 1895. It was not until around 1926 that biocompatible stainless steels were developed, while more contemporary biocompatible implant alloys such as Co-based and Ti-based alloys were developed between 1936 and 1950, respectively (Navarro et al., 2008). Gomez and Morcuende (2005) have reviewed early attempts at hip arthroplasty dating back to the 1700 s while Knight et al. (2011) discuss total hip arthroplasty over 100 years. Over the past several decades, total joint replacement involving knees and hips have accelerated to millions of such surgeries world-wide annually (Walker, 1978; Yaszemski et al., 2003; Katti, 2004; Wang et al., 2011; Kremer et al., 2015). Dental replacement has also gained prominence along with other oral and maxillofacial implants (Brunski, 2000).

While commercial implant appliances are often very reliable, some knee and hip replacements lasting in excess of 25 years, they are usually solid metals or alloys having a modulus of elasticity (Young's modulus) far in excess of the surrounding bone. This creates a condition known as stress shielding where bone resorption or bone density reduction occurs around the implant, such as hip stems in the femur, where bone will remodel in response to loads it is placed under (Ridzman et al., 2007). For example, popular implant alloys such as Co-Cr-Mo and Ti-6Al-4V have a Young's modulus of 210 GPa and 110 GPa, respectively (Navarro et. al., 2008). These stiffnesses are much greater than trabecular (or soft) bone regime which can range from roughly 0.1 to 2 GPa in contrast to hard, cortical (or outer) bone which ranges from 18 to 22 GPa. Niinomi (1998) has described Ti-alloys such as Ti-35Nb-5Ta-7Zr having a Young's modulus of 55 GPa, and Hao et al. (2007) have described a Ti-25Nb-4Zr-8Sn alloy having a modulus of elasticity of ~42 GPa. While these lower stiffness alloys can reduce the stress shielding for bone, solid stems or plates require screws and/or cement to stabilize the implant, and there is no bone tissue ingrowth and no other biological function.

Over the past decade, considerable effort has been directed at the creation of more biocompatible implants, especially improving biome-

☆ Dedicated to my long-time friend and colleague, Professor Marc A. Meyers on the occasion of his 70th birthday.

* Correspondence address: Department of Metallurgical, Materials and Biomedical Engineering, The University of Texas at El Paso, El Paso, TX 79968 USA.
E-mail address: lemurr@utep.edu.

http://dx.doi.org/10.1016/j.jmbbm.2017.02.019
Received 1 January 2017; Received in revised form 15 February 2017; Accepted 17 February 2017

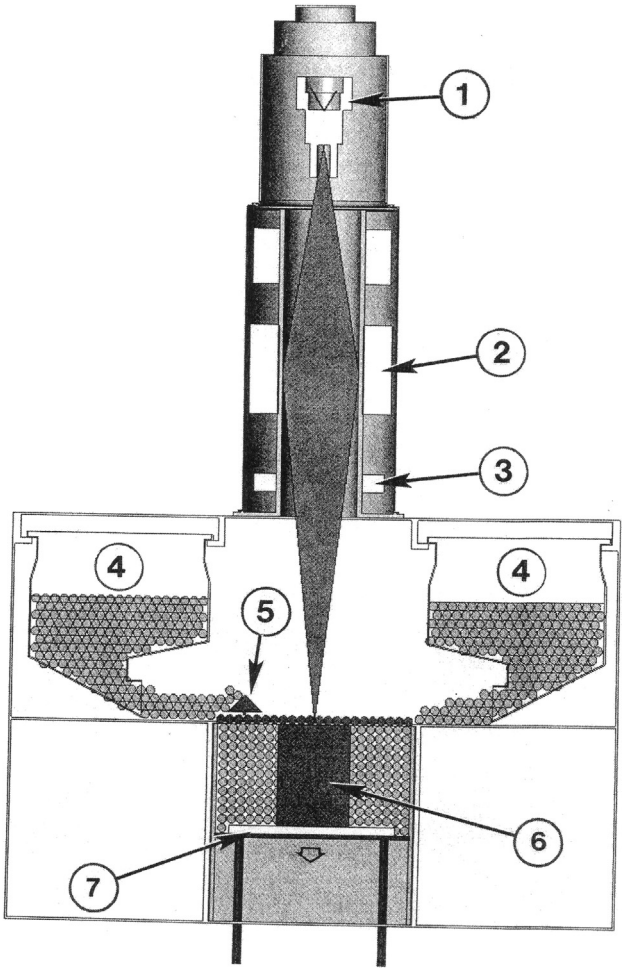

Fig. 1. EBM system schematic: (1) electron gun; (2) beam focusing lens; (3) beam scan; (4) Powder cassettes; (5) layer rake; (6) building product; (7) build table which is lowered with each processed layer.

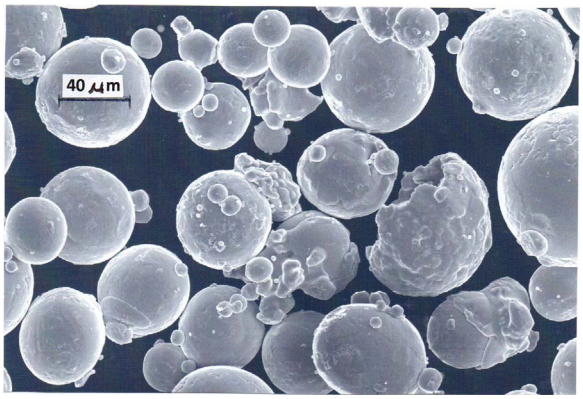

Fig. 2. Example of Co-Cr-Mo pre-alloyed powder for EBM processing. Average powder diameter is ~40 μm.

chanical compatibility through porous material and structure design (Karageorgio and Kaplan, 2005; Greisamer, 2007; Pruitt and Chakravartula, 2011). The commercial application of tantalum mesh to hip sterns along with similar surface porosity design strategies allowed for some bone ingrowth and limited stress shielding relief. However, more important implant improvements began to emerge with the advent of commercial electron and laser beam selective melting of metal and alloy powder beds to fabricate complex reticulated mesh and stochastic, open-cellular foam structures. This allowed for

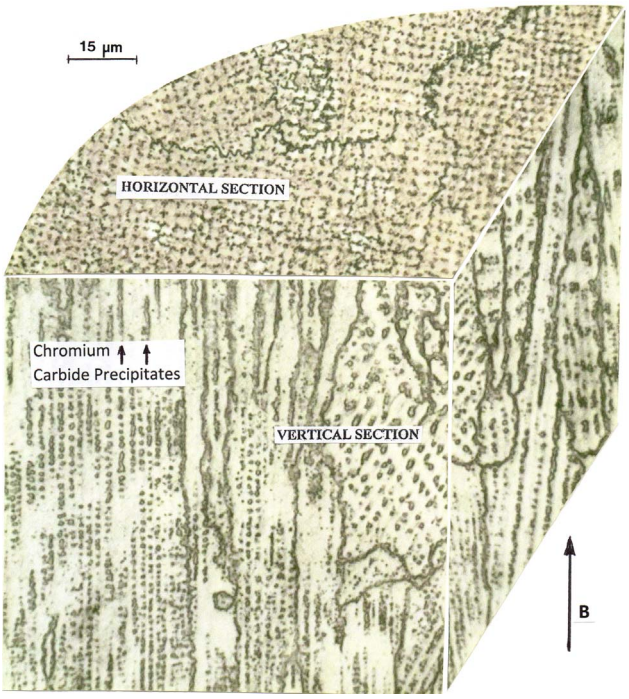

Fig. 3. Optical microscope 3D composite section showing an EBM-fabricated Co-Cr-Mo component having directionally grown grains and columns of Cr_{23} C_6 precipitates oriented in the build direction (arrow).

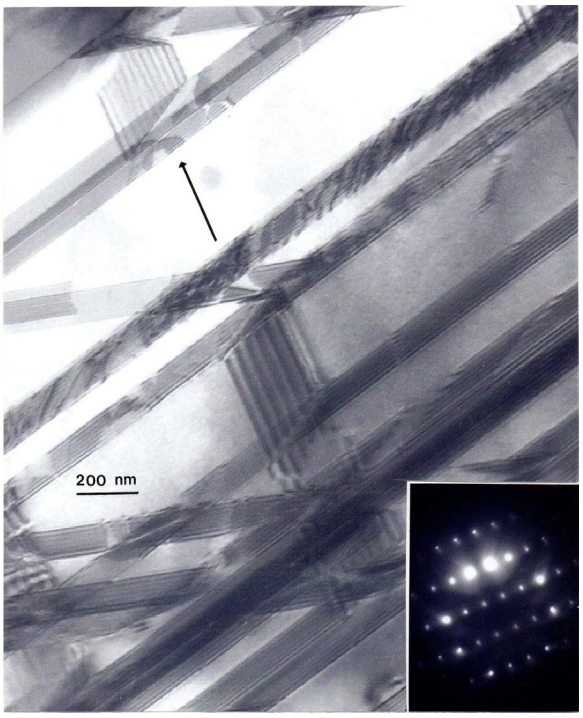

Fig. 4. TEM bright-field image showing stacking faults in Hiped (ASTM-F75 schedule) EBM component shown in Fig. 3. The selected-area electron diffraction pattern insert (bottom left) shows a [112] surface orientation. The arrow in the image shows the [1$\bar{1}$0] trace direction for one set of stacking faults on the (111) plane in the fcc matrix.

patient-specific implant scaffolds which provided bone-compatible elastic modulus design as well as optimized porosities promoting bone cell ingrowth, and the prospects for implant vascularization (Murr et al., 2009, 2010a, 2010b; Horn et al., 2014; Nune et al., 2015; Kumar et al., 2016).

This paper reviews these contemporary design strategies for devel-

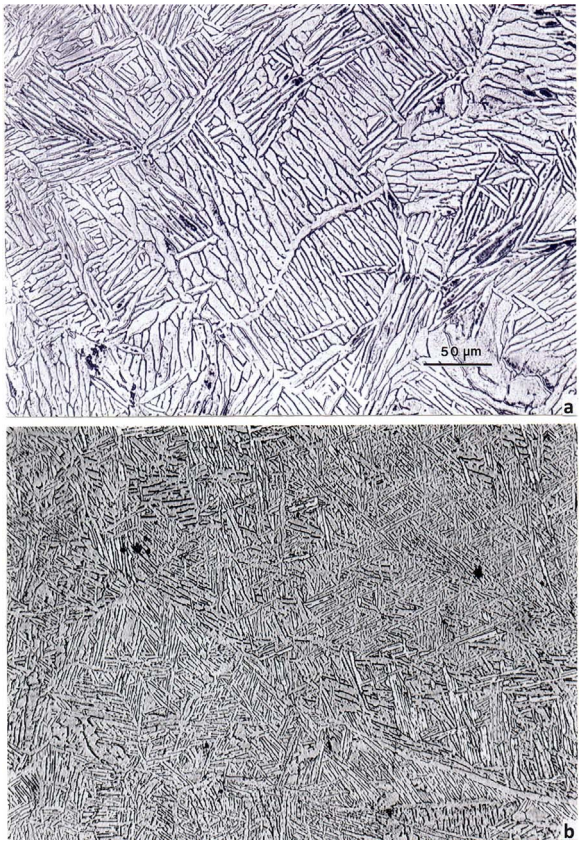

Fig. 5. Optical micrographs showing EBM-fabricated Ti-6Al-4V components. (a) 300 mm/s @ 6 mA melt scan. Residual hardness ~3.4 GPa (Vickers). (b) 400 mm/s @ 4 mA melt scan. Residual hardness ~4.3 GPa (Vickers). The alpha grains are white while the dark regions surrounding the grains are beta. The magnification in (b) is the same as shown by the magnification marker in (a).

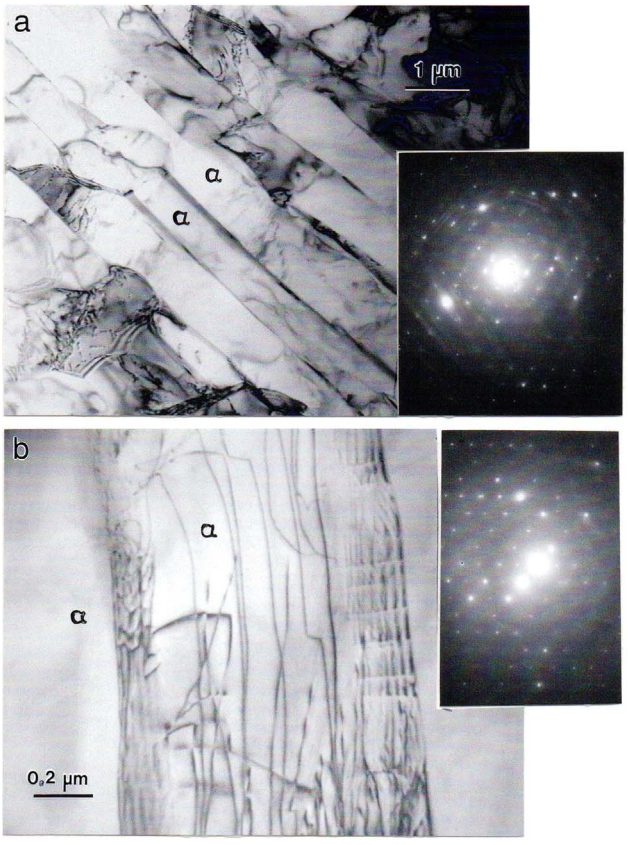

Fig. 6. TEM images for small size (thickness) alpha-grain structure in Fig. 5(b). (a) α-β (dark) phase structure. hcp selected-area electron diffraction pattern insert. (b) Magnified TEM image showing dislocation structure in alpha (α) grains. Selected-area electron diffraction pattern insert shows hcp structure.

oping porous, patient specific and application specific implants using electron beam melting (EBM) fabrication. The microstructures and mechanical properties of more conventional Ti-6Al-4V and Co-Cr-Mo biomedical alloys are initially compared with EBM-fabricated alloys. Principles relating to the mechanics of 3D-cellular materials originally described by Gibson and Ashby (1982) are reviewed along with compression strength and fatigue issues as these relate to dynamic implant design and applications (Pruitt and Chakravartula, 2011; Li et al., 2012, 2014). Finally, examples of EBM-fabricated, open-cellular implants and their applications as well as biocompatibility observations and clinical trials are presented.

2. Electron beam melting (EBM): microstructures and mechanical behavior of Ti-6Al-4V and Co-Cr-Mo components

Fig. 1 illustrates a schematic view of the EBM system (ARCAM A2) used to fabricate solid and open-cellular (mesh and foam) biomedical alloy examples to be described in this paper. The system in Fig. 1 consists of an electron gun (1) operated nominally at a 60 kV accelerating potential. Electrons are focused into a beam using a magnetic lens system at (2), and the focused beam is scanned over the prepared (raked) powder bed using magnetic scan coils at (3). Precursor, pre-alloyed powder, such as the Co-Cr-Mo (Co-29Cr-6Mo-0.22 C) powder shown in Fig. 2, is gravity fed from cassettes (4) and raked (5) into a smooth, partially packed powder bed. The scanned beam selectively melts sections of the powder bed according to computer-aided design (CAD) software. Spherical, size-distributed, atomized powders illustrated typically in Fig. 2 are designed to fill interstitial volumes in the raked layer, which is normally pre-heated using rapid-raster beam scanning prior to a slower, higher beam

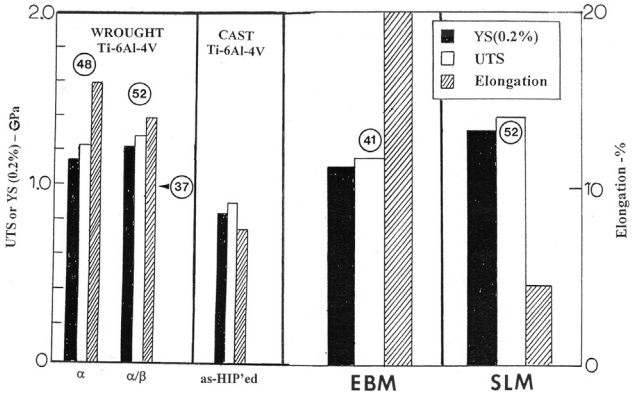

Fig. 7. Mechanical property comparison for commercial and EBM-fabricated Ti-6Al-4V and Co-Cr-Mo alloys. Co-Cr-Mo components are denoted by ASTM-F75 standard. From Murr (2015a). Note Co-Cr-Mo data is to right of arrow in center white the Ti-6Al-4V data is to the left.

current melt scan. Melted layers generally grow epitaxially on the previous layer (Murr, 2015a, 2015b; Basak and Das, 2016). This repeated melt-solidification, layer-by-layer fabrication differs significantly from more conventional cast solidification and directional solidification, often implicit in directional microstructures or architectures. This feature is illustrated in the image composite reproduced in Fig. 3 for Co-Cr-Mo solid component EBM fabrication which shows columns of $Cr_{23}C_6$ precipitates generally arranged in the build direction, B (Gaytan et al., 2010). While $Cr_{23}C_6$ precipitates are also observed in cast Co-Cr-Mo, they are usually more homogeneously dispersed or observed to grow in grain boundaries. Commercial, cast or wrought Co-Cr-Mo implant components eliminate these precipitates by

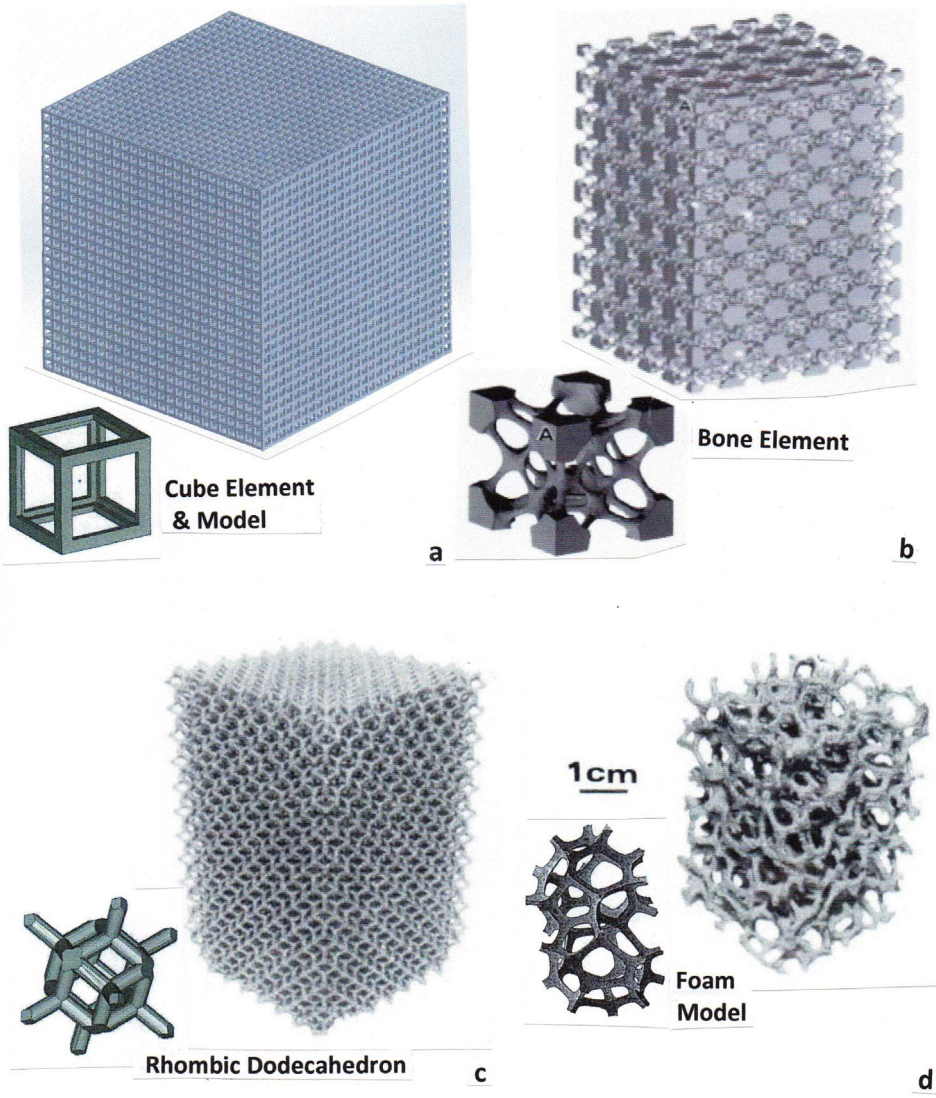

Fig. 8. EBM-fabrication/build elements, software models and fabricated products. (a) Cubic unit cell. (b) Materialize (TM) bone unit cell and software model. (c) Rhombic dodecahedron element and EBM Ti-6Al-4V product. (d) Foam model and EBM fabricated Ti-6Al-4V foam product.

HiP (hot isostatic processing) according to ASTM F75 schedule treatment. This consists in heating at 1200 °C for 4 h in 10^3 bar Ar followed by quench from a homogenizing temperature of 1220 °C for 4 h. This treatment dissolves the $Cr_{23}C_6$ precipitates and leaves a notable stacking-fault structure contributing to desirable strength and ductility. EBM fabricated products exhibit the same microstructure development with ASTM-F75 schedule treatment as illustrated in the typical transmission electron microscope (TEM) image shown in Fig. 4 (Gaytan et al., 2011). Gaytan et al. (2010) have shown similar microstructural features for mesh structures of Co-Cr-Mo.

Perhaps one of the most important alloys or alloy components fabricated by EBM has been Ti-TAl-4V, which has become one of the principle biomedical (implant) materials (Navarro et al., 2008; Murr et al. 2009; Wang et al., 2011). In contrast to EBM-fabricated Co-Cr-Mo shown in Fig. 3, Ti-6Al-4V does not normally result in directional microstructures or architectures for EBM-fabricated products, but exhibits lenticular or similar, elongated alpha-phase (hcp) grains surrounded by a thin zone of beta phase (bcc) material as shown in Fig. 5. Fig. 5(a) shows a large (thick) alpha grain structure which arises for very slow beam melting while Fig. 5(b) illustrates a more refined alpha grain structure which results by more rapid cooling. These microstructural differences are reflected in residual microindentation (Vickers) hardnesses: 3.4 GPa in Fig. 5(a) and 4.3 GPa in Fig. 5(b). The microstructure of Fig. 5(b) is illustrated in more detail in the TEM images of Fig. 6, exhibiting α-plates as thin as 1 μm. These microstructures and associated mechanical properties are similar in some respects to commercial cast or wrought products in the case of Ti-6Al-4V, while EBM-fabricated Co-Cr-Mo products generally exceed the cast, Hiped Co-Cr-Mo alloy. Even the EBM-fabricated and Hiped product (as illustrated in Fig. 4) exhibits a yield stress twice that for the commercial ASTM-F75 product used in the manufacture of biomedical implant appliances (Odahara et al., 2008; Patel et al., 2012). Fig. 7 illustrates these comparative mechanical behaviors for Ti-6Al-4V and Co-Cr-Mo alloys. Also of particular note in Fig. 7 is the nearly triple elongation (or ductility) of EBM (z)+HIP for Co-Cr-Mo versus the commercial ASTM-F75 alloy; which may be due in part to the columnar grain structure in the former. In contrast, however, the Young's modulus (E) for Co-Cr-Mo alloy is around 210 GPa compared to 110 GPa for Ti-6Al-4V; providing particular challenges for stress shielding in softer bone, or the transition between the trabecular bone regime and the outer cortical bone regime, where nominally E≅2 to 10 GPa.

Like titanium alloys, tantalum forms a passive oxide layer which provides good corrosion resistance (Eliaz, 2012; Matassi et al., 2013). In addition, Almanza et al. (2017) have shown that porous Ti-6Al-4V and Co-Cr-Mo alloys exhibit corrosion features essentially the same as

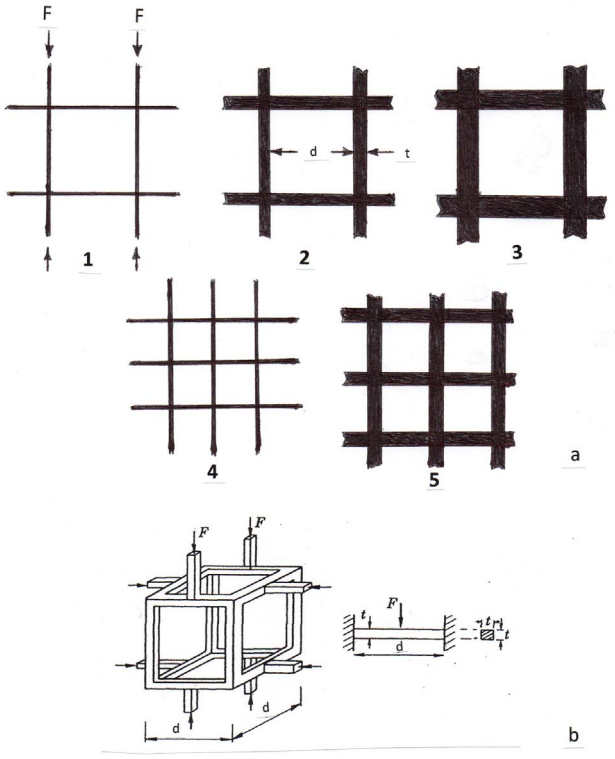

Fig. 9. Cubic structure loading and strut dimensions. (a) Compressive force (F) loading of simple cubic mesh struts having thickness, t, and length d, corresponding to open-cellular pore size. In (1)–(3), d is constant while t increases. In (1) and (4), (2) and (5), t is constant while d decreases, differently. (b) Simple cubic structure loaded with force, F, in the strut center to create bending in contrast to buckling in (a) – (1).

Fig. 10. Upper femur section showing intramedullary (trabecular bone) structure consisting of soft bone tissue and matrix. Google image.

commercial, solid alloys.

3. Porous implant biomechanical compatibility strategies for bone replacement

The ability and utility of using high Young's modulus, high density metals such as tantalum, especially in hip stem implants as noted above, is predicated upon the fabrication of porous appliances. Porosity of course reduces the nominal density, and porosity is related to Young's modulus as discussed by Gibson and Ashby (1982): Young's modulus, E, decreases with an increase in porosity. Porosity (P) is also related to the density or relative density (ρ/ρ_s):

$$P = (1 - \rho/\rho_s) \times 100\%, \quad (1)$$

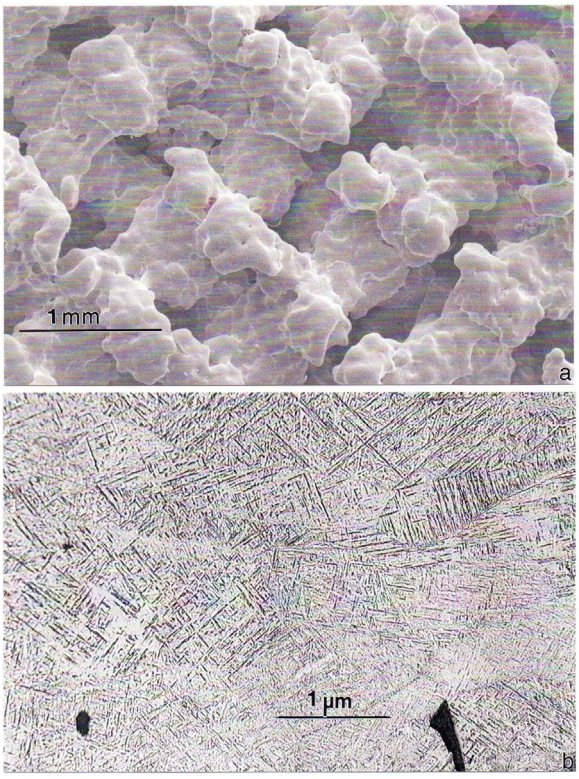

Fig. 11. (a) Thin, irregular particle strut structure for EBM-fabricated Ti-6Al-4V cubic mesh product. (b) Optical microscope image showing thin, alpha-prime (α′) hcp phase characterizing the mesh strut microstructure in (a) as a result of rapid cooling. Residual Vickers microindentation hardness ~4.8 GPa.

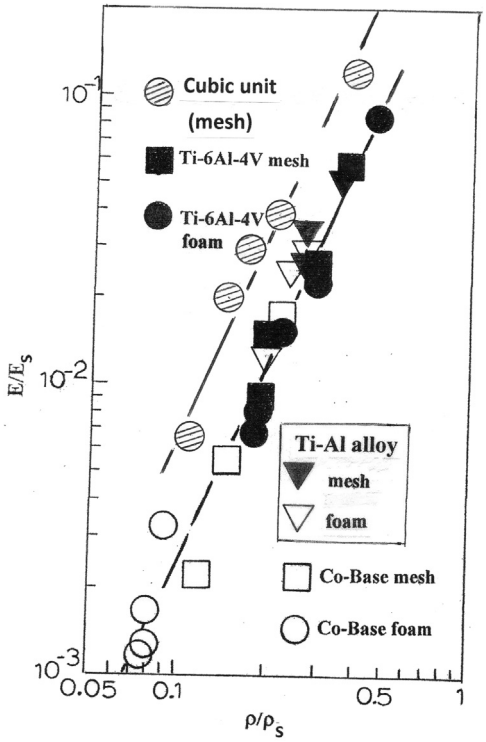

Fig. 12. Relative Young's modulus (stiffness) (E/E_s) versus relative density (ρ/ρ_s) plots for Ti-6Al-4V (E_s=110 GPa, ρ_s=4.43 g/cm^3) Co-Cr-Mo 8 (E_s=210 GPa, ρ_s=8.44 g/cm^3) and Ti-Al alloy (44Ti – 39Al – 7(Ni, Nb)) (E_s=135 GPa, ρ_s=4.11 g/cm^3) reticulated mesh and foam samples fabricated by EBM. Cubic unit mesh data from Li et al. (2014) is for Ti-6Al-4V. Ti-Al mesh and foam data adapted from Hernandez et al. (2012). Ti-6Al-4V mesh and foam data adapted from Murr et al. (2010a, 2010b).

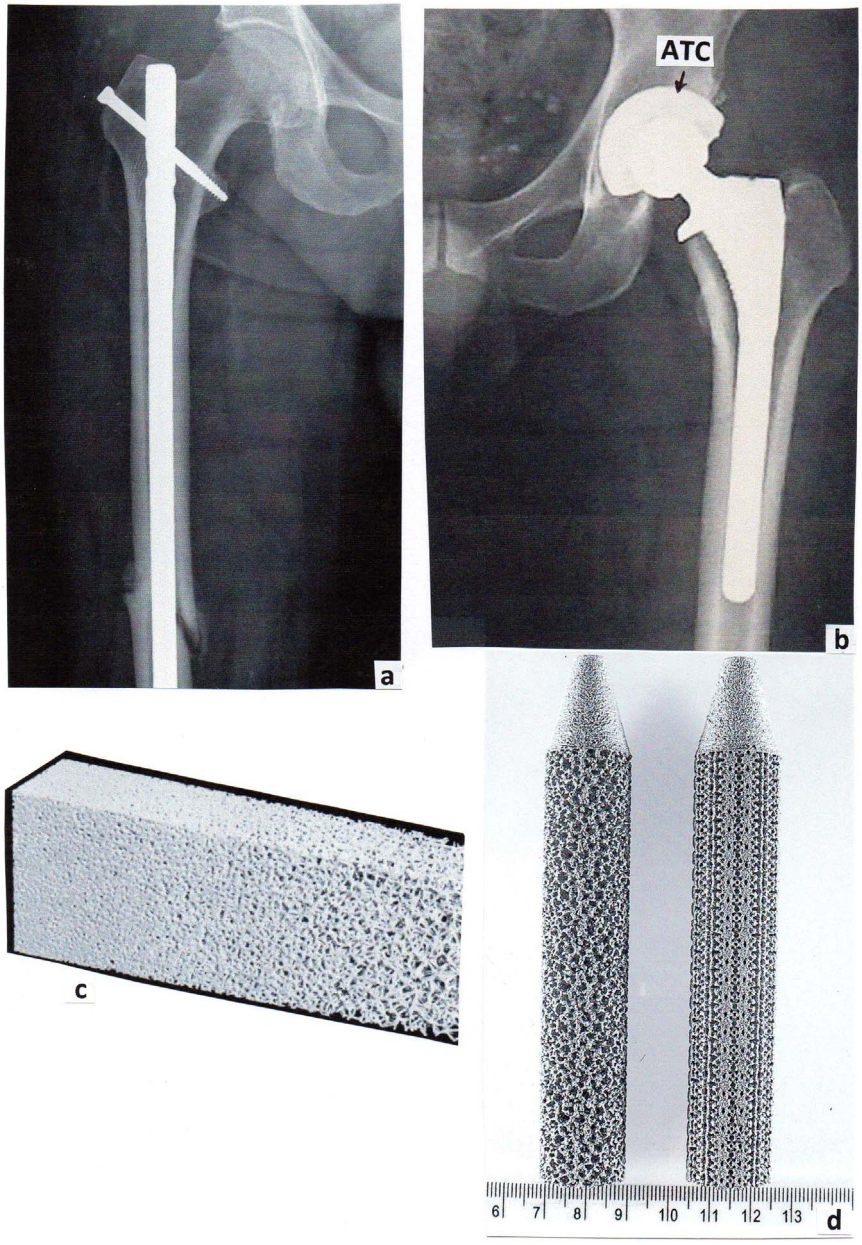

Fig. 13. Examples of conventional, solid Ti-6Al-4V hip rods (a) and hip stem (b) in contrast to graded porosity (c) and functionally porous Ti-6Al-4V stems fabricated by EBM (d). (d) corresponds to open-cellular models illustrated in Fig. 14(b) and (d), left-to-right, respectively. Note in (b) the porous Ti-6Al-4V acetabular cup (ATC) composing the total hip replacement components.

where ρ is the cellular structure component density while ρ_s is the solid component (full) density.

While porosity or porous products have been variously created by a variety of novel techniques, the advent of laser and electron beam melting technologies using CAD – directed melt strategies has provided the means to fabricate an array of reticulated mesh as well as open-cellular stochastic foam and related complex structures, where porosity and associated mechanical behavior, including Young's modulus or elastic modulus, E, can be controlled. Reticulated mesh structures are fabricated using unit cell (or element) geometries and CAD software such as Solid Works (Dassault Systemes, Waltham, MA); with unit cell models converted to standard tessellation format (STL) and using processing software (Magics, Materialise, Plymouth, MI) in either laser or electron beam melting systems (as illustrated in Fig. 1). Fig. 8 illustrates several common unit cell formats and more extended models or actual components fabricated by EBM using the Magics/Materialize software. Fig. 8(a) represents the simplest, cubic unit cell or build element for a reticulated mesh and an extended model composed of these elements, while Fig. 8(b) shows a somewhat more complex (bone) unit cell and an extended model. Fig. 8(c) illustrates a rhombic dodecahedron unit cell and an EBM fabricated Ti-6Al-4V sample, while Fig. 8(d) show a foam model section representing an isotropic, random, open-cellular foam constructed by *Surface Evolver* (Bakke, 1992) and an EBM fabricated Ti-6Al-4V foam. Foam units consisting of larger foam sections have also been constructed for micro-CT scans of natural or other fabricated metal foams (Murr et al., 2010b).

It can be observed in Fig. 8 that both the bone unit cell and rhombic dodecahedron unit cell in Fig. 8(b) and (c), respectively are geometrically closely associated with the stochastic foam shown in Fig. 8(d). Fig. 9 illustrates that variations in the strut cross-section (or thickness, t) as well as the strut length can adjust the porosity and pore size (d′), which in Fig. 9(a) can be represented nominally by, or related to, the strut length (d); i.e. $d' \propto d$. Considering that the 2D model cells in Fig. 9(a) are characteristic of the simple cubic unit cell in Fig. 8(a), the

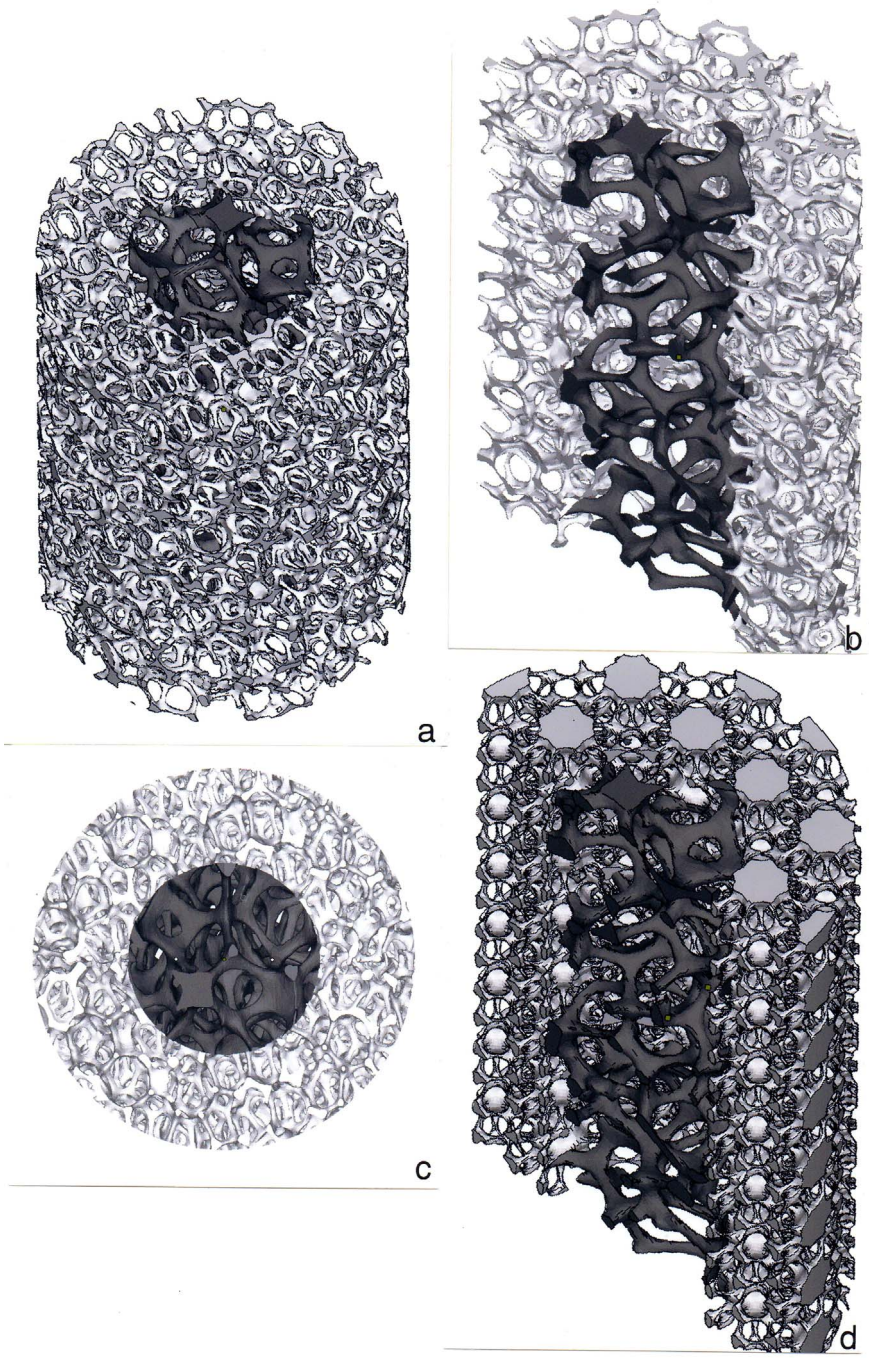

Fig. 14. EBM – CAD models representing functional open-cellular structures shown in Fig. 13(d). (a) and (b) show full view and section having inner and outer foam density (and porosity) differences to ideally match soft (inner) and hard (outer) bone for EBM-fabricated rods or stems as shown in Fig. 13(d). (c) and (d) show longitudinal cross-sections representing Fig. 13(d). From Murr (2015a, 2015b), courtesy of Springer.

applied compressive force or load, F, on a strut having a cross-section, A, can be expressed as

$$F = \sigma d^2/4, \quad (2)$$

where σ is the stress on the mesh, and d is the strut length (Fig. 9(a)). For a strut with uniform cross section, its linear elastic deformation, Δ d, is (Beer et al., 2001):

$$\Delta d = Fd/E_sA = \sigma d^3/4E_st^2, \quad (3)$$

where E_s is the solid material Young's modulus or elastic stiffness. Since $E=\sigma/\varepsilon$ (strain) by Hooke's law, the Young's modulus becomes

$$E\alpha\ 4\sigma E_sdt^2/\sigma d^3 = C_1E_s(t/d)^2, \quad (4)$$

where C_1 is a constant. For the simple cubic cell in Figs. 8(a) and 9(a):

$$\rho/\rho_s\ \alpha\ (t/d)^2 \quad (5)$$

and Eq. (4) can be written

$$E/E_s = C_1(\rho/\rho_s) \quad (6)$$

For the modified cube element shown in Fig. 9(b), where the load is applied to bend the strut horizontally as opposed to vertical deflection as in Fig. 9(a), the Young's modulus, E or stiffness is given by (Gibson and Ashby, 1982):

$$E = CE_s(t/d)^4, \quad (7)$$

substituting Eq. (5), Eq. (7) becomes

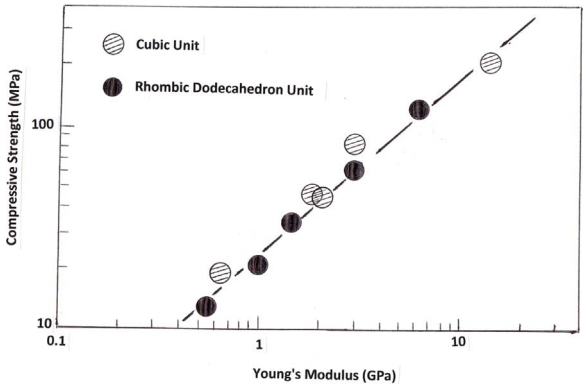

Fig. 15. Plot of compressive stress versus Young's modulus for Ti-6Al-4V open-cellular components fabricated by EBM using cubic and rhombic dodecahedron build elements (unit cells). Data from Li et al. (2014).

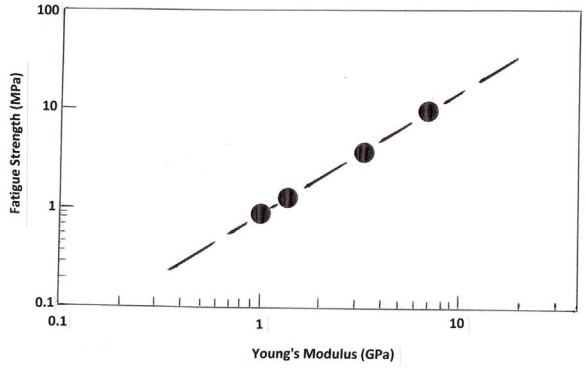

Fig. 16. Plot of fatigue strength versus Young's modulus for Ti-6Al-4V reticulated mesh components fabricated by EBM using a rhombic dodecahedron build element (Fig. 8c). Data from Li et al. (2014).

$$E/E_s = C\,(\rho/\rho_s)^2\,, \tag{8}$$

where C is often 0.9 (Prawoto, 2012). Eq. (8) has also been shown to apply to cancellous (hard) or trabecular (soft) bone as well (Keaveny and Hayes, 1993).

While the unit cell shown in Fig. 9(a) characterizes Fig. 8(a), the modified cubic unit cell shown in Fig. 9(b) approximates the loading of the rhombic dodecahedron unit cell in Fig. 8(c) as well as the more complex cubic bone unit cell in Fig. 8(b). Gibson and Ashby (1982) demonstrate that Eq. (8) is also characteristic of stochastic, open-cellular foams as well. Eq. (8) is in fact often referred to as the Gibson-Ashby equation, and Babaee et al. (2012) have recently shown that from a detailed theoretical approach the elastic and plastic deformation for open-cellular rhombic dodecahedron structures obey this equation in all three directions.

It can be observed from Eqs. (1), (5), and (8), that for open-cellular, complex mesh-resembling foam structures can be selectively designed for specific porosities (p), pore size (d), and stiffness (E) to accommodate specific bone stiffness or Young's modulus as well as the pore size for an implant. While stiffness adjustment relieves stress shielding in bone, the pore size is important for optimum bone cell ingrowth, which is generally in the range of 200–400 μm (Karageorgio and Kaplan, 2005; Kuman et al., 2016). Implicit in Fig. 9(a) is the fact that strut thickness (t) can be held constant while d is changed, d can be constant while t is varied, or both t and d can change independently. In most porous metal or alloy structure fabrications to be considered herein, the mesh thickness, t, varied between 0.5 and 1 mm (Murr et al. 2010a; Li et al., 2014). It should also be noted that while d in Fig. 8a represents the pore size in a simple cube- face geometry shown, the actual pore size is usually some fraction of the strut dimension, d. For foam structures, the ligament dimensions can vary with pore size or

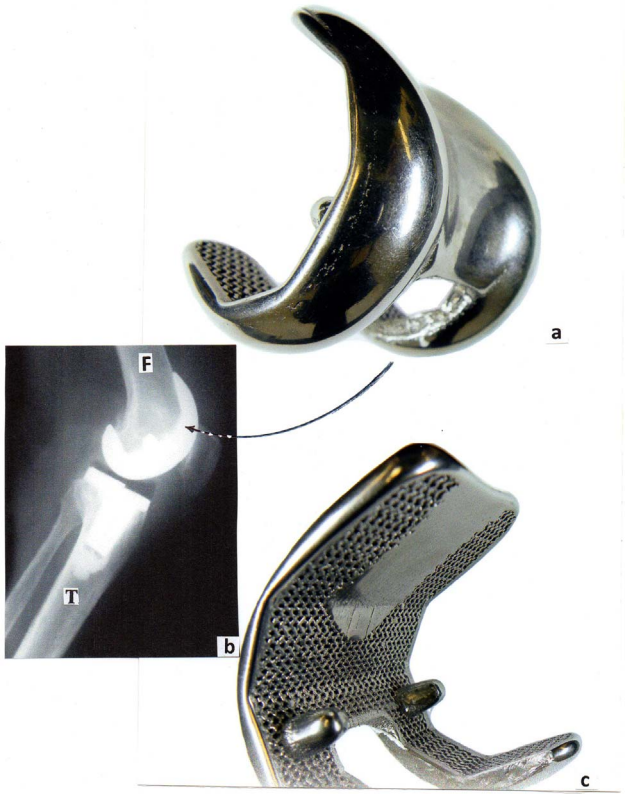

Fig. 17. Co-Cr-Mo EBM-fabricated femoral appliance in total knee replacement (implant). (a) and (c) show outside (contact surface) and reticulated mesh inside (femoral end). (b) Shows typical X-ray for total knee replacement. F and T designate femur and tibia, respectively. Mesh strut dimension (pore size) is ~1 mm. The highly cross-linked polyethylene component separating the femoral and tibial appliances is invisible to X-rays, and not observed in (b).

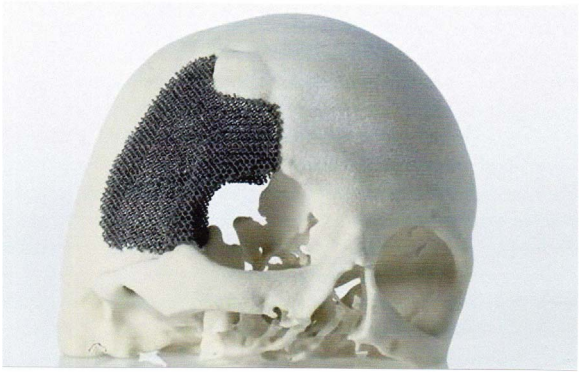

Fig. 18. Rhombic dodecahedral element reticulated Ti-6Al-4V mesh skull replacement prototype fabricated by EBM.

nominal pore size, which as noted is optimally around 200–400 μm,because in order to produce a continuous bone cell regime within the open-cellular structures, the cells must be able not only to adhere to the struts or ligaments but also bridge the pores through various cytoplasmic extensions to promote migration through the interconnecting porous architectures (Karageorgio and Kaplan, 2005; Nune et al., 2014, 2015; Kumar et al. 2016). Horn et al. (2014 have recently studied porosity, pore size, strut size and relative density for EBM-fabricated Ti-6Al-4V mesh structures utilizing the rhombic dodecahedron unit cell (Fig. 8(c)) as a build element. Incorporating related Ti-6Al-4V work by others, they illustrated that relative the Young's modulus and relative density were related by the Gibson-Ashby equation (Eq. (8)), and that relative density (ρ/ρ_s) and pore size (d) generally followed a non-linear behavior implicit in Eq. (5): ρ/ρ_s

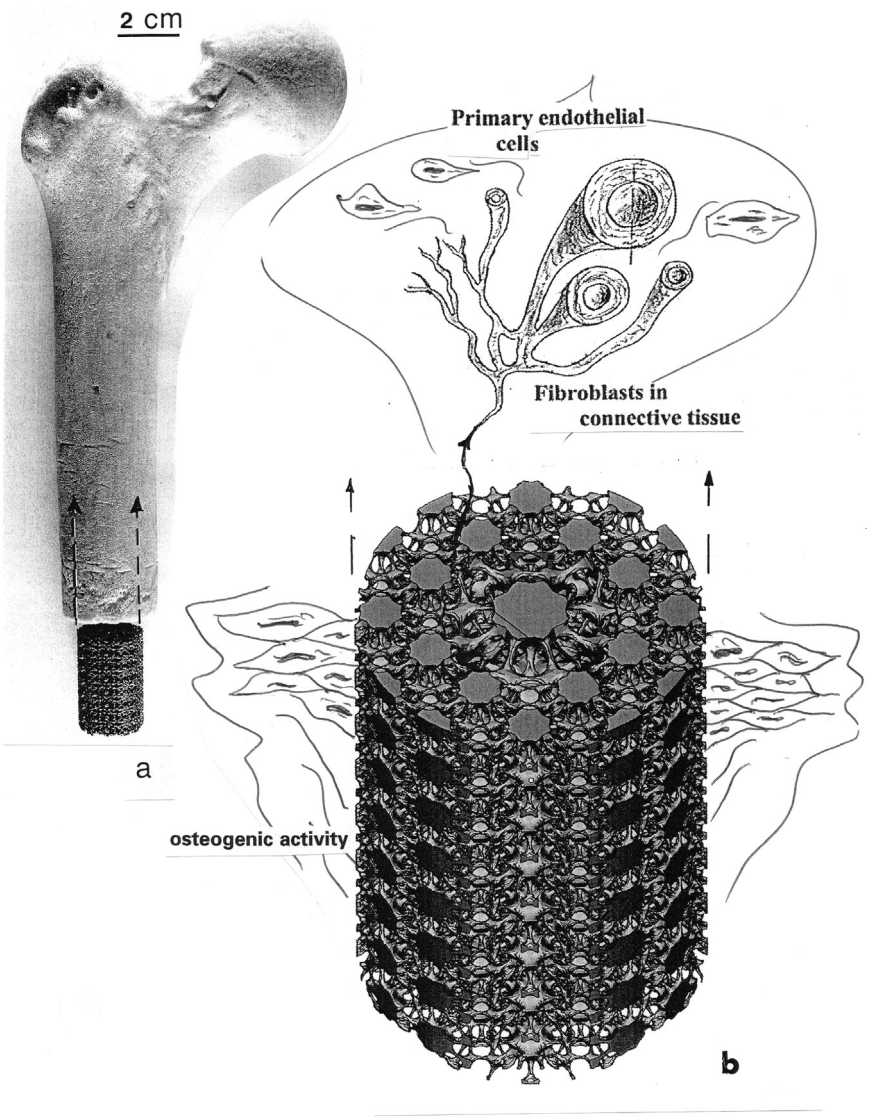

Fig. 19. Living implant concept illustrations. (a) EBM-fabricated Ti-6Al-4V femoral stem section fabricated using a graded "bone" element (unit cell) (Fig. 8b). (b) Blood vessel development and bone cell (osteoblast) migration and growth in a collagen-endothelial cell – signaling molecule – connective tissue matrix inserted within and maturing in the open-cellular structure. From Murr (2015a, 2015b), courtesy of Springer.

decreasing as pore size increased, non-linearly. Strength was also noted to be influenced by strut size (t in Fig. 9) as well as porosity (Eq. (1)). In this regard, the compressive stress, σ_c, for mesh structures based on the rhombic dodecahedron unit cell and open-cellular foams is generally expressed by (Gibson and Ashby, 1982; Li et al., 2014):

$$\sigma_c/\sigma_y = C'(\rho/\rho_s)^{1.5}, \quad (9)$$

where σ_y is the optimum compressive yield stress and C′ is a constant. Similarly, Keaveny and Hayes (1993) have shown from measured data that the ultimate compressive strength, U_c, for cancellous (or trabecular) bone can be expressed by:

$$U_c = C''(\rho/\rho_s')^2, \quad (10)$$

where C′′ is a constant, and ρ_s' represents the upper-most density for trabecular bone. Fig. 10 shows a section of the upper femur which consists mainly of graded trabecular bone composing the intramedullary region between the outer, cortical (hard) bone shell. The compressive stress-strain diagram generally shows that the compressive stress for the trabecular region in Fig. 10 exhibits a maximum stress (σ_c) ranging from 10 to 40 MPa at maximum strains of ~ 22%, while the outer cortical bone has a maximum σ_c of ~190 MPa with maximum strains around 2%, exhibiting a correspondingly brittle-like behavior (Keaveny and Hayes, 1993; Currey, 2006).

For high load-bearing bone structures in the legs, implant optimization, such as intramedullary rods or hip stems, must have relatively high porosity in order to match the soft (trabecular) bone stiffness (Eq. (8)) while maintaining requisite compressive strength (Eq. (9)); as well as energy (and impact) absorption, and fatigue resistance. These are somewhat mutually opposing requirements which in these circumstances are only optimized through mechanical property compromise. It is also interesting to note that for most successful Ti-6Al-4V open-cellular implant designs, small strut or ligament dimensions give rise to rapid process cooling in EBM fabrication, and this leads to either a significantly reduced alpha phase dimension or lenticular (alpha) plate thickness as illustrated in Fig. 5, or alpha prime (α′) platelet formation as shown in Fig. 11. In contrast to Fig. 5(b), where the alpha phase thickness is roughly 1 μm, the alpha-prime platelet thickness (the width of the dark lines) in Fig. 11(b) is roughly 50 nm; and the corresponding microindentation (Vickers) hardness is ~4.8 GPa. Recalling that for many metals and alloys, hardness is roughly three times the yield stress, the compressive stress for cellular Ti-6Al-4V implants might correspondingly be as much as 45% greater than solid, fully dense Ti-6Al-4V. Fig. 11(a) also shows that for EBM fabrication,

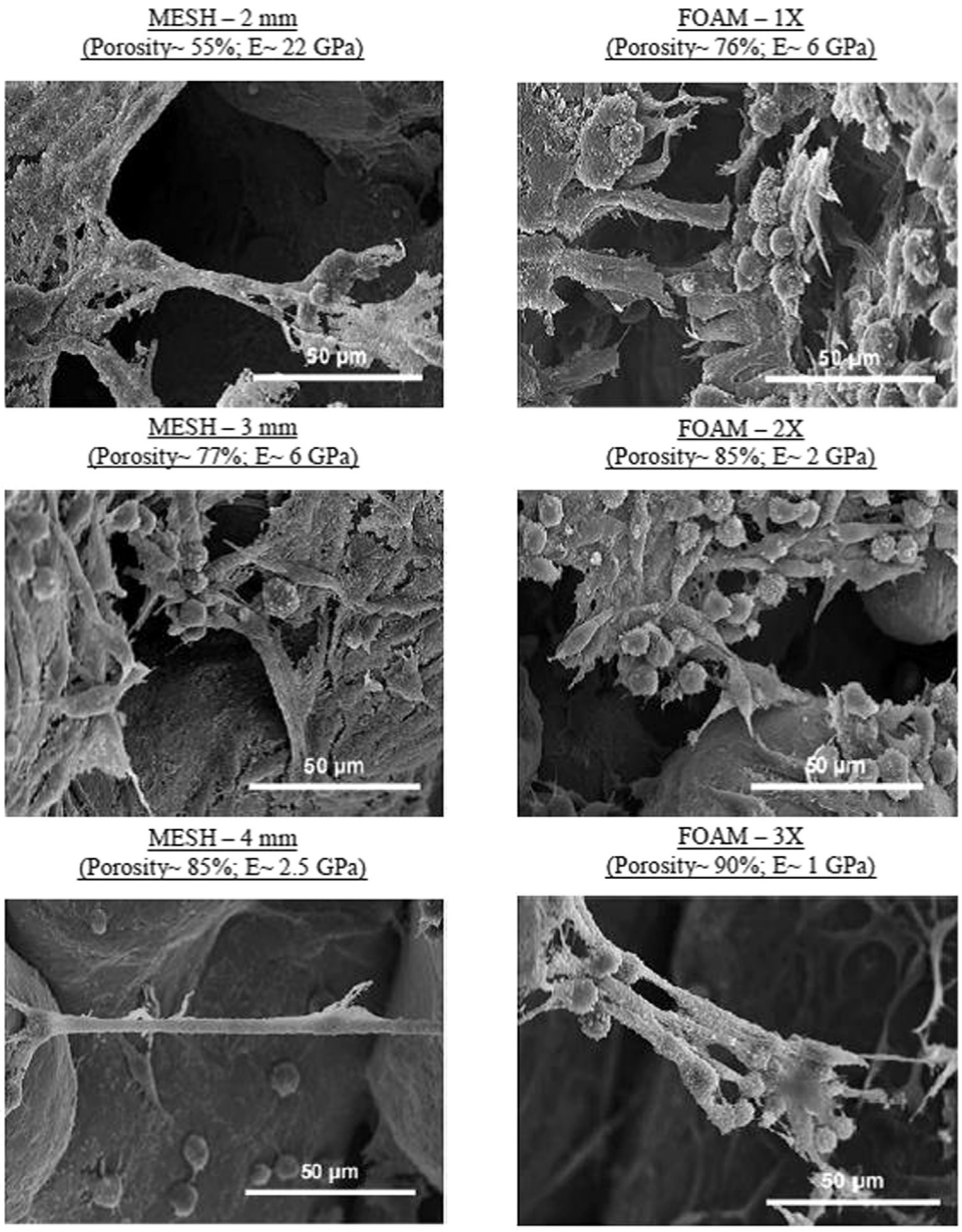

Fig. 20. Scanning electron micrographs showing cellular (pre-osteoblast) ingrowth and interconnectivity (bridging pores) on open-cellular Ti-6Al-4V cubic mesh and foam EBM components having properties noted; after 3 weeks incubation. Adapted from Nune et al. (2015).

powder size and process parameters (such as melt scan and beam current) can limit the strut or ligament dimensions. In addition, strut or ligament "roughness" as apparent in Fig. 11(a) can, on the one hand, promote bone cell adhesion while possibly compromising cracking or failure (even fatigue failure) on the other hand.

Fig. 12 provides a starting point for porous (cellular) implant design strategy and illustrates that there is good correspondence with the Gibson-Ashby equation (Eq. (8)) for a number of unit cell build element geometries (Fig. 8) and metals and alloys, based on experimental data from Murr et al. (2010a, 2016) and Li et al. (2014) for Ti-6Al-4V and Co-Cr-Mo alloys, and Hernandez et al. (2012) for TiAl (44Ti-39Al-7Ni-4Nb-4Cr-2Mo); for mesh and foam samples. Dynamic Young's moduli reproduced in Fig. 12 were measured by means of a damping analyzer which measures resonant frequency (Li et al. 2014). Fig. 13(a) and (b) illustrate X-ray images for a conventional intramedullary rod (Ti-6Al-4V) and a total hip replacement appliance, including a femoral stem, respectively, while Fig. 13(c) shows a graded, foam component closely matching the femoral bone section shown in Fig. 10. Fig. 13(d) shows EBM-fabricated, functional stem implants using the design models shown in Fig. 14; with Fig. 14(b) and (d) corresponding to the fabricated alloys on the left and right, respectively, in Fig. 13(d). For these porous stems, the internal foam in Fig. 14(b) might average the trabecular (soft) bone regime in the femur (Fig. 10), roughly 1–2 GPa, while the outer foam would more closely match the cortical bone regime, roughly 10–20 GPa. This would correspond to a relative Young's modulus averaging ~1.3×10^{-2} for the trabecular (inner) foam in Fig. 14(b) and ~1.3×10^{-1} for the cortical (outer foam in Fig. 14(b). These values of relative modulus (E/E_s) correspond to relative densities (ρ/ρ_s) of ~0.2 to 0.3 and ~0.4 to 0.7, respectively, for the inner and outer foams in Fig. 14(b) for a Ti-6Al-4V stem (Fig. 13(d), left component). Considering the relationship between compressive strength and Young's modulus measured for Ti-6Al-4V mesh products reproduced from data of Li et al. (2014) in Fig. 15, it is observed that the corresponding inner foam in Fig. 14(b) would have a compressive strength of ~20 to 30 MPa, essentially matching the strength of trabecular bone (Keaveny and Hayes, 1993). Similarly, the outer foam

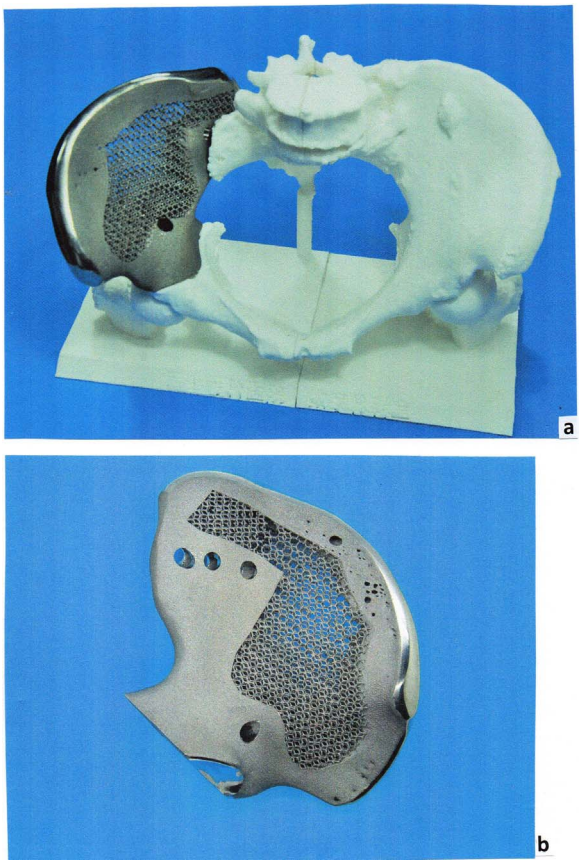

Fig. 21. Ti-6Al-4V porous pelvic girdle, right wing iliac bone replacement implant fabricated by EBM. (a) Pelvic, iliac bone replacement implant fitted to skeletal model. (b) Pelvic, iliac bone replacement in (a) enlarged and rotated for fabrication details. Courtesy of Dr. S.J. Li, Institute of Metals Research (IMR), Shenyang, China.

design modulus of ~15 GPa from the outer foam in Fig. 14(b) would ideally result in a compressive strength of ~130 MPa in Fig. 15; roughly 30% lower than the maximum cortical bone compressive strength of ~190 MPa (Keaveny and Hayes, 1993). For relative densities of 0.3 and 0.7 used in the above design scenario for trabecular and cortical bone matching, respectively, the corresponding porosities (Eq. (1)) become ~70% and 30%; which are near the 30–90% porosity for trabecular and 5–30% for cortical bone, respectively. In this single example for a Ti-6Al-4V foam implant following the build model shown in Fig. 14(b), the associated open-cellular foam pore sizes will be similar to those in natural trabecular and trabecular/cortical transition bone (Fig. 10). Consequently, bone cell adhesion and migration should be facilitated as discussed previously. Furthermore, if such femoral implant stems were utilized in situations where patient gait (especially walking gait abnormalities) and body weight might exacerbate fatigue strength or fatigue endurance limits, the outer foam regime, designed for a Young's modulus of ~15 GPa, would ideally have a fatigue strength of ~40 MPa according to the experimental data (Li et al., 2012; Zhao et al., 2016) reproduced in Fig. 16. In addition, the designed porosities should also allow for impact and energy absorption approximating natural bone regimes. Impact (energy) absorption and fatigue issues will also be more extreme for the foot bone (second metatarsal) having a high arch, especially for active adults who run extensively. The ability to fabricate patient specific porous implants for such reconstruction applications may be particularly advantageous.

Over the past decade, tens of thousands of acetabular cups (Fig. 13b) having designed porosity for EBM-fabricated Ti-6Al-4V of around 30% have been utilized in total hip replacements worldwide (Kremer et al., 2015). Similar design strategies have been employed for femoral appliances of Co-Cr-Mo (ASTM F75) in total hip and knee replacements as shown in Fig. 17. Co-Cr-Mo implants and components have been utilized in hip and knee replacements because of the much higher hardness, especially for metal-on-metal (MoM) devices, where high hardness and correspondingly excellent wear and corrosion resistance are required. Commercial forming routes for Co-Cr-Mo orthopaedic alloys can produce hardnesses as high as 12 GPa (Patel et al., 2012), in contrast to Ti-6Al-4V with nominal hardnesses of around 4 GPa. Co-Cr-Mo devices have similar advantages in total knee replacements where, as shown in Fig. 17(b), the femoral component contacts a highly cross-linked polyethylene pad at the top of the tibial insert; replacing the meniscus. Like the hip, knee implant components are subjected to a complex array of bearing stresses, fatigue, and impact stresses. Dalal et al. (2012) and Scharf et al. (2014) among others, have examined Co-Cr-Mo related toxicity especially for particles produced in MoM devices in comparison with Ti and Zr alloys, concluding that Co-Cr nano particles in particular were far more toxic.

There are situations where implants are not subjected to significant and rather continuous bearing or other stresses, and can serve as bone replacement. This is especially true for skull bone-related implants as illustrated in Fig. 18. Head (or skull) bone in adults has a nominal Young's modulus of ~6.5 GPa, while it can be as low as ~1 GPa for infants. The bone thickness for the skull can also vary from ~6 to 10 mm in adults (Sarkar et al. 2004; Currey, 2006). Of course there are instances when static and dynamic loads might be experienced by the skull, especially in the case of sports-related impact or falls (Sarkar et al., 2004).

4. Porous implant performance and trials

Two decades ago, the performance of metal-on-metal (MoM) hip replacement devices exhibited device longevities lasting around 15 years (Shinar and Harris, 1998; Teloken et al., 2002), while in more recent times, this has nearly doubled as a consequence of porous device fabrication, such as acetabular cups, by EBM, and the use of highly cross-linked ultrahigh molecular weight polyethylene (UHMWPE) inserts to eliminate MoM problems such as debris formation (Klenerman, 2012; Kremer et al., 2015), and cementless total hip arthroplasty (Ohishi et al., 2016). Similar results have been observed for total knee replacement devices (Fig. 17), where the Young's modulus for the highly cross-linked UHMWPE is much higher than natural cartilage, and its higher hardness and associated hydrophobicity contribute to intrinsic lubrication and correspondingly low wear rates, and related lower debris formation. Reduction in wear rate also reduces osteolysis and associated aseptic loosening of implant components: failure of the bond between the component and bone in the absence of infection (Ren et al., 2013; Athanasou, 2016). However, infection has also been a major issue in implant surgeries, even though antibiotics are routinely added to cements to avoid infection, which can also lead to component loosening and failure (Dapunt et al., 2016). The use of porous implants avoids cement and provides for long-term infection reduction by seeding the porous components with appropriate antibiotics (Murr, 2013; Benzuihout et al., 2015; Rapel et al., 2016).

Porous, open-cellular implant structures illustrated in Figs. 13(d) and 14 for femoral stems and rods as well as bone replacements shown in Fig. 18 are especially amenable to producing a living or functional bone replacement through enhanced osteoblast and vascularization seeding (Matena et al., 2015; Kang et al., 2016; Kumar et al., 2016). This concept is illustrated in Fig. 19. The implications of Fig. 19 are, as recently discussed by Li et al. (2017), that porous implants can be infused with a suitable bio-matrix consisting of collagen, proteins, pre-osteoblast cells, endothelial cells, growth factors, signaling molecules, and other appropriate function promoters such as deferoxamine mesylate (DFM) or deferoxamin (DFD) to promote angiogenesis by inducing hypoxia (Chen et al., 2013). Similarly, Veschini et al. (2007) and more recently Correa et al. (2017) have reported that endothelial

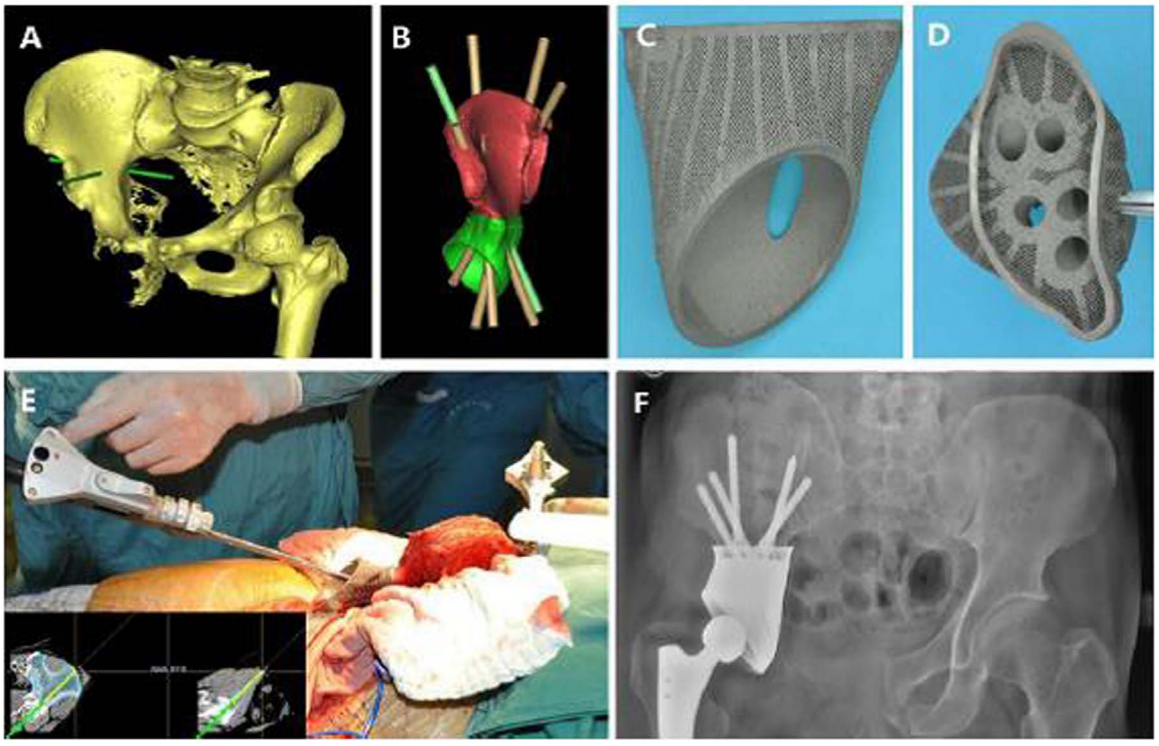

Fig. 22. Surgical example of customized periacetabular partial pelvic reconstruction. A – Reconstructed 3D pelvic tumor model. B – Virtual model of acetabular prosthesis. C – Anterior of customized Ti-6Al-4V acetabular prosthesis fabricated by EBM. D – Superior view of implant. E – Prosthesis implantation and fixation by computer-aided surgical navigation system. F – X-ray image showing excellent alignment and osseointegration after 18 months postoperatively. From Li et al. (2017). Courtesy of X.K. Li and Z. Guo, Department of Orthopedics, Xijing Hospital, Fourth Military Medical University, Xi'an, China; and J. Wiley.

cells form capillaries in gel when exposed to DFM. Correa et al. (2017) also noted promotion of osteoblast proliferation by DFM hypoxia induction, while Nune et al. (2014, 2015) have demonstrated the potential of bone morphogenetic prokin (BMP-2) in imparting osteoinductive capability to 3D-printed scaffolds due to the unique self-assembled structure of BMP-2 that effectively communicates with osteoblast cells.

Fig. 20 reproduces some observations of mouse pre-osteoblast cell ingrowth and interconnectivity by bridging pores in modified cubic Ti-6Al-4V mesh (Fig. 9a) and foam structures fabricated by EBM. The mesh designations in Fig. 20 show strut lengths of 2, 3, and 4 mm which for the modified cubic structure corresponded to average pore sizes of 300, 600, and 900 μm, respectively as determined from scanning electron microscope (SEM) images. The corresponding foam samples in Fig. 20 correspond to ~300, 600, and 900 μm pore sizes for 1×, 2×, and 3× foam designations, respectively. The corresponding mesh and foam densities and associated dynamic (Young's) moduli are also noted in Fig. 20. The SEM observations in Fig. 20 correspond to a 21 day incubation period after the open-cellular structures were treated with BMP-2 solution and seeded with mouse pre-osteoblast cells. Following three weeks incubation as shown in Fig. 20, osteoblast cell seeding efficiency was observed to be ~80% for the 2 mm mesh, 70% for the 3 mm mesh, and ~57% for the 4 mm mesh. Correspondingly, cell seeding efficiency for the 1×, 2×, and 3× foams (Fig. 20) was observed to be 57%, 47% and ~30%, respectively. Cell proliferation rate (percent/day) was observed to be around 46% for all open-cellular structures except for the 1 mm (300 μm pore size) mesh which was ~53% (Nune et al., 2014, 2015). Consequently, while Fig. 20 attests to the attachment and migration of osteoblast cells even in large pore-size open-cellular structures, there is an increased efficiency for the smaller, 300 μm pore size. Of course the infusion of open-cellular implant structures with DNA-speciated osteoblast, endothelial, and other cell types in a hydrogel-collagen matrix as noted above to assure rapid bone formation and vascularization within the metal implant scaffold during surgical insertion, would conceptually enhance this function as implicit in Fig. 19. Related work by Lewallen et al. (2015) reached similar conclusions. It is also notable to point out that Nune et al. (2014, 2015) also observed a corresponding increase in calcium phosphate mineralization with cell proliferation and migration in Fig. 20, consistent with hydroxyapatite formation and availability for bone formation.

While in-vitro studies of bone-cell ingrowth and vascularization are indicative of the potential for the use of open-cellular implants for a wide range of bone replacements, there are mounting examples of successful surgical applications of these appliances. Certainly Ti and Ti-alloy (Ti-6Al-4V) dental implants provide an example, where concerns for stress shielding issues have also begun to promote porous metal or alloy tooth designs (Wally et al., 2015). Maxillofacial implants (Fig. 18) are especially promising (Peel and Eggbeer, 2016) as well as 3D reconstruction in craniofacial defects (deMoraes et al., 2015). Thousands of acetabular revision arthroplasty examples (Fig. 13b) attest to porous metal implant applications (Pulido et al., 2011; Ranawat et al., 2016). Fig. 21 illustrates an application of a pelvic girdle, right wing(ala) ilium(iliac bone) reconstructive Ti-6Al-4V, EBM-fabricated implant in a stereolithography-fabricated, polymer pelvic girdle. Fig. 22 shows surgical planning and results for a customized, Ti-6Al-4V pelvic tumor and acetabulum reconstruction and prosthesis design by EBM fabrication for a 35-year-old male. The prosthesis was designed to eliminate stress shielding and optimize bone cell ingrowth using an open-cellular structure. The sequence in Fig. 22 shows positioning and satisfactory fixation of the implant after 18 months (Li et al., 2017). Many thousands of similar examples of 3D-printed, porous metal implants, including spinal implants, have undergone successful clinical trials over the past 5 years at Peking University Third Hospital in Beijing, Xijing Hospital, Fourth Military Medical University, Xi'an (Li et al., 2017), and other locations in China where porous Ti-6Al-4V implant structures are often fabricated in-house using EBM (Cai, 2015).

5. Summary and conclusions

After providing an initial historical perspective regarding implant bone replacements, this review compared microstructures and mechanical properties for popular Ti-6Al-4V and Co-Cr-Mo implant appliance component fabrication using conventional cast and wrought technologies, and electron beam melting (EBM) - additive manufacturing technologies. These alloys are among the oldest and most effective, biocompatible implant materials used in hip and knee component replacements, bone stems and rods, and the like. Additive manufacturing using EBM allows a wide range of open-cellular implant designs to be fabricated in order to eliminate stress shielding and associated bone resorption (reduction in bone density), and the ability to utilize cementless surgical insertion as well as the enhanced, associated osseointegration and bone formation. The ability to fabricate graded porosity can functionalize the implant like natural bone. Porous implant impregnation and seeding with a collagen-based matrix incorporating endothelial and other associated, speciated cells, proteins, growth factors and signaling molecules can allow for enhanced vascularization and bone growth within the porous structures. Incorporating appropriate antibiotic agents within these porous structures can also prevent infection and sustain long-term infection protection. These measures will also assure notable reduction in septic and aseptic loosening of implants.

The ability to design and fabricate personalized, patient-specific, open-cellular (porous) implants using EBM and related additive manufacturing techniques and the integration of various biological, chemical, and mechanical methods will likely yield more effective strategies to improve long-term clinical outcomes. This is particularly important because of the proliferation of implant surgeries among younger populations, as well as the increasingly larger life expectancies of older adults undergoing implant surgeries. These features exemplify typical strategies in materials science and engineering which strive to enhance material performance and life expectancy (Murr, 2015a, 2015b).

I am grateful for the many examples and contributions by students and colleagues which are acknowledged in the figure captions or in the references cited throughout the paper.

References

Almanza, E., Penz, M.J., Rodriguez, N.A., Murr, L.E., Calliari, I., 2017. Corrosion resistance of Ti-6Al-4V and ASTM F75 alloys processed by electron beam melting. J. Mater. Res. Technol., (Submitted for publication).

Athanasou, N.A., 2016. The pathobiology and pathology of aseptic implant failure. Bone Jt. Res. 5, 162–168.

Babaee, S., Jahromi, B.H., Ajdari, A., Nayeb-Hashemi, H., Vaziri, A., 2012. Mechanical properties of open-cell rhombic dodecahedron cellular structures. Acta Mater. 60, 2873–2885.

Bakke, K.A., 1992. The surface evolver. Exp. Mech. 1, 141–165.

Basak, A., Das, S., 2016. Epitaxy and microstructure evolution in metal additive manufacturing. Ann. Rev. Mater. Res. 46, 125–149.

Beer, F.P., Johnson, E.R., DeWolf, J.T., 2001. Mechanics of Materials 3rd ed.. McGraw-Hill, New York.

Benzuihout, M.B., Dimitrou, D.M., Dicks, L.M.T., 2015. Titanium-based hip stem with drug delivery functionality through additive manufacturing. Biomed. Rev. Int., 134093.

Brunski, J.B., Puleo, D.A., Nanci, A., 2000. Biomaterials and biomechanics of oral and maxillofacial implants: current status and future developments. J. Oral Maxillofac. Implant. 15, 15–46.

Cai, H., 2015. Application of 3D printing in orthopedics: status quo and opportunities in China. Ann. Transl. Med. 3 (Suppl. 1), S12–S15.

Chen, L.-L., Huang, M., Tan, J.-Y., Chen, X.-Ti, Lei, L.-H., Wu, Y.-M., Zhang, D.-Y., 2013. PI3K/AKT pathway involvement in the osteogenic effects of osteoblast culture supernatants on preosteoblast cells. Tissue Eng. Part A 19 (19–20), 2226–2232.

Correa, V.L., Murr, L.E., Garza, K.L., 2017. Vascularization in Interconnected 3D Printed Ti-6Al-4V Foams With Hydrogel Matrix for Biomedical Bone Replacement Implants (In preparation).

Currey, J.D., 2006. Bones: Structure and Mechanics. Princeton University Press, Princeton.

Dalal, A., Pawar, V., McAllister, K., Weaver, C., Hallab, N.J., 2012. Orthopedic implant cobalt-alloy particles produce greater toxicity and inflammatory cytokines than titanium alloy and zirconium alloy-based particles in vitro, in human osteoblasts, fibroblasts and macrophages. J. Biomed. Mater. Res. Part A 100A, 2147–2158.

Dapunt, U., Radzuweit-Mihaljevic, S., Lehner, B., Haensch, G.M., Ewerbeck, V., 2016. Bacterial infection and implant loosening in hip and knee arthroplasty: evaluation of 209 cases. Materials 9, 871–881.

deMoraes, P.H., Olate, S., Cantin, M., Assis, A.F., Santos, E., deOliveira Silva, F., deOliveira Silva, L., 2015. Anatomical reproducibility through 3D printing in cranio-maxillo-facial defects. Int. J. Morpol. 33 (3), 826–830.

Eliaz, N. (Ed.), 2012. Degradation of Implant Materials. Springer Science and Business, New York.

Gaytan, S.M., Murr, L.E., Martinez, E., Martinez, J.L., Machado, B.I., Ramirez, D.A., et al., 2010. Comparison of microstructures and mechanical properties for solid and mesh cobalt-base alloy prototypes fabricated by electron beam melting. Metall. Mater. Trans. A41, 3216–3227.

Gaytan, S.M., Murr, L.E., Ramirez, D.A., Machado, B.I., Martinez, E., Hernandez, D.H., et al., 2011. A TEM study of cobalt-base alloy prototypes fabricated by EBM. Mater Sci. Appl. 2, 355–363.

Gibson, L.J., Ashby, M.F., 1982. The mechanics of three-dimensional cellular materials. Proc. R. Soc. Lond. Math. Phys. Sci. 383, 43–49.

Gomez, P.F., Morcuende, J.A., 2005. Early attempts at hip arthroplasty 1700s to 1950s. Iowa Orthop. J. 25, 25–29.

Greisamer, R.P., 2007. Applications of porous tantalum in total hip arthroplasty. J. Am. Acad. Orthop. Surg. 15 (3), 137–7145.

Hao, Y.L., Li, S.J., Sun, S.Y., Zheng, C.Y., Yang, R., 2007. Elastic deformation behavior of Ti-24 Nb-4Zr-7.9Sn for biomedical applications. Acta Biomater. 3, 277–286.

Hernandez, J., Murr, L.E., Amato, K.N., Martinez, E., Shindo, P.W., Terrazas, C.A., Rodriguez, E., et al., 2012. Microstructures and properties of a superalloy powder mixture processed by electron beam melting. J. Mater. Sci. Res. 1 (3), 124–144.

Horn, T.J., Harrysson, O.L.A., Marcellin-Little, D.J., West, H.A., Lascelles, B.D.X., Aman, R., 2014. Flexural properties of Ti6Al4V rhombic dodecahedron open cellular structures fabricated with electron beam melting. Addit. Manuf. 1–4, 2–11.

Kang, H.-W., Lee, S.J., Ko, I.K., Kengia, C., Yoo, J.J., Atala, A., 2016. A 3D bioprinted system to produce human-scale tissue constructs with structural integrity. Nat. Biotechnol. 34, 312–319.

Karageorgio, V., Kaplan, D., 2005. Porosity of 3D biomaterial scaffolds and osteogenesis. Biomaterials 26, 5474–5491.

Katti, K.S., 2004. Biomaterials in total joint replacement. Colloids Surf. B. Biointerfaces 39 (3), 133–142.

Keaveny, T.M., Hayes, W.C., 1993. Mechanical properties of cortical and trabecular bone. In: Hall, B.K. (Ed.), Bone 7. CRC Press, Boca Raton, FL, 285–344.

Klenerman, L. (Ed.), 2012. The Evolution of Orthopaedic Surgery. Royal Society of Medicine Press, Ltd, London.

Knight, S.R., Aujla, R., Biswas, S.P., 2011. Total hip arthroplasty – over 100 years of operative history. Orthop. Rev. 3 (2), 1–16.

Kremer, M.H., Larson, D.R., Crawson, C.S., Krema, W.K., Washington, R.E., Steiner, C.A., et al., 2015. Prevalence of total hip and knee replacement in the United States? J. Bone Jt. Surg. Am. 97 (17), 1386–1397.

Kumar, A., Nune, K.C., Murr, L.E., Misra, L.D.K., 2016. Biocompatibility and mechanical behavior of three-dimensional scaffolds for biomedical devices: process-structure-property paradigm. Int. Mater. Rev. 61 (1), 20–45.

Lewallen, E.A., Riester, S.M., vanWijnen, A.J., 2015. Biological strategies for improved osseointegration and osteoinduction of porous metal orthopedic implants. Tissue Eng. Part B Rev. 21 (2), 218–230.

Li, S.J., Murr, L.E., Cheng, X.Y., Zhang, Z.B., Hao, Y.L., Yang, R., Medina, F., Wicker, R.B., 2012. Compression fatigue behavior of Ti-6Al-4V mesh arrays fabricated by electron beam melting. Acta Mater. 60, 793–802.

Li, S.J., Xu, O.S., Wang, Z., Hou, W.T., Hao, Y.L., Yang, R., Murr, L.E., 2014. Influence of cell shape on mechanical properties of Ti-6Al-4V meshes fabricated by electron beam melting method. Acta Biomater. 10, 4537–4547.

Li, S.J., Li, X.K., Hou, W.T., Nune, K.C., Misra, R.D.K., Correa-Rodriguez, V.L., Guo, Z., Hao, Y.L., Yang, R., Murr, L.E., 2017. Fabrication of Open-Cellular (Porous) Titanium Alloy Implants: Osseointegration, Vascularization and Preliminary Human Trials (In preparation).

Matassi, F., Botti, A., Sirleo, L., Carulli, C., Innocenti, M., 2013. Porous metal for orthopedics implants. Clin. Cases Miner. Bone Metabol. 10 (2), 111–115.

Matena, J., Petersen, S., Giescke, M., Kampman, A., Teske, M., Beyerbach, M., Escober, H.M., et al., 2015. SLM produced porous titanium implant improvements for enhanced vascularization and osteoblast seeding. Int. J. Mol. Sci. 16, 7478–7592.

Murr, L.E., 2013. Some comments on orthopaedic implant infection: biomaterials issues. J. Biotechnol. Biomater. 3 (3), 1000e119, (3 pages).

Murr, L.E., 2015a. Metallurgy of additive manufacturing: examples from electron beam melting. Addit. Manuf. 5, 40–53.

Murr, L.E., 2015b. Handbook of Materials Structures, Properties, Processing and Performance 2. Springer International Publishing, Switzerland.

Murr, L.E., 2016. Frontiers of 3D printing/additive manufacturing: from human organs to aircraft fabrication. J. Mater. Sci. Technol. 32, 987–995.

Murr, L.E., Gaytan, S.M., Medina, F., Lopez, H., Martinez, E., Machado, B.I., Hernandez, D.H., Martinez, L., Lopez, M.I., Wicker, R.B., Bracke, J., 2010a. Next-generation biomedical implants using additive manufacturing of complex, cellular and functional mesh arrays. Philos. Trans. R. Soc. A 368, 1999–2032.

Murr, L.E., Amato, K.N., Li, S.J., Tian, Y.X., Cheng, X.Y., Gaytan, S.M., et al., 2010b. Microstructure and mechanical properties of open-cellular biomaterials prototypes for total knee replacement implants fabricated by electron beam melting. J. Mech. Biomed. Mater. 4, 1396–1411.

Murr, L.E., Quinones, S.A., Gaytan, S.M., Lopez, M.I., Rodela, A., Martinez, E.Y., Hernandez, D.H., Martinez, E., Medina, F., Wicker, R.B., 2009. Microstructure and mechanical behavior of Ti-6Al-4V produced by rapid-layer manufacturing, for

biomedical applications. J. Mech. Behav. Biomed. Mater. 2, 20–32.
Navarro, M., Michiardi, A., Castano, O., Planell, S.A., 2008. Biomaterials in orthopaedics. J. R. Soc. Interface 5, 1137–1158.
Niinomi, M., 1998. Mechanical properties of biomedical titanium alloys. Mater. Sci. Eng. A 243, 231–236.
Nune, K.C., Kumar, A., Murr, L.E., Misra, R.D.K., 2015. Interplay between self-assembled structure of bone morphogenetic protein-2 (BMP-2) and osteoblast functions in three-dimensional titanium alloy scaffolds: stimulation of osteogenic activity. J. Biomed. Mater. Res. Part A 104A, 517–532.
Nune, K.C., Misra, R.D.K., Gaytan, S.M., Murr, L.E., 2014. Biological response of next-generation of 3D Ti-6Al-4V biomedical devices using additive manufacturing of cellular and functional mesh structures. J. Biomater. Tissue Eng. 4 (10), 755–771.
Odahara, T., Matsumoto, H., Chiba, A., 2008. Mechanical properties of biomedical Co-33Cr-5Mo-0.3N alloy at elemental temperatures. Mater. Trans. 49 (9), 1963–1969.
Ohishi, M., Nakashima, Y., Yamamoto, T., Motomura, G., Fukushimio, J.-I., Kohno, Y., Iwamoto, Y., 2016. Cementless total hip arthroplasty for patients previously treated with femoral osteotomy for hip dysplasia: the incidence of periprosthetic fracture. Int. Orthop. 40 (8), 1601–1606.
Pal, T.K., 2015. Fundamentals and history of implant dentistry. J. Int. Clin. Dent. Res. Organ 7 (Suppl. 8l), S6–S12.
Patel, B., Favaro, G., Inam, F., Reece, M.J., Angadji, A., Bonfield, W., Huang, J., Edirisinghe, M., 2012. Cobalt-based orthopaedic alloys: relations hip between forming route, microstructure and tribological performance. Mater. Sci. Eng. C 32, 1222–1229.
Peel, S., Eggbeer, D., 2016. Additively manufactured maxillofacial implants and guides. Rapid Prototype J. 22 (1), 189–199.
Prawoto, Y., 2012. Seeing auxetic materials from the mechanics point of view: a structural review of negative Poisson's ratio. Comput. Mater. Sci. 58, 140–153.
Pruitt, L.A., Chakravartula, A.M., 2011. Mechanics of Biomaterials: Fundamental Principles for Implant Design. Cambridge University Press, Cambridge.
Pulido, L., Rachala, S.R., Cabenela, M.E., 2011. Cementless acetabular revision: past, present, and future. Revision total hip arthroplasty: the acetabular side using cementless implants. Int. Orthop. 35 (2), 289–298.
Ranawat, A.S., Meftah, M., Thomas, A.O., Thippanna, K.K., Ranawat, C.S., 2016. Use of oversized highly porous cups in acetabular revision. Orthopedics 39 (2), e301–e306.
Rapel, J., Holsdniy, M., Goodman, S.B., Heilshorn, S.C., 2016. Multifunctional coatings to simultaneously promote osseointegration and prevent infection of orthopaedic implants. Biomaterials 84, 301–314.
Ren, K., Dusad, A., Zhang, Y., Wang, D., 2013. Therapeutic intervention for wear debris-induced aseptic implant loosening. Acta Pharm. Sin. B 3 (2), 76–85.
Ridzman, M.I.Z., Shuito, S., Hassan, A.Y., Shokri, A.A., 2007. Problem of stress shielding and improvement to the hip implant designs: a review. J. Med. Sci. 7 (3), 460–467.
Sarkar, S., Majundar, S., Roychowdhury, A., 2004. Response of human head under static and dynamic load using finite element method. Trends Biomater. Artif. Organs 17 (2), 130–134.
Scharf, B., Clement, C.C., Zolla, V., Perino, G., Yan, B., Elci, S.G., Purdne, E., Goldring, S., Macaluso, F., Gobelli, N., Vachet, R.W., Santambrogio, L., 2014. Molecular analysis of chromium and cobalt-related toxicity. Sci. Rep. (Nat.) 4 (5729). http://dx.doi.org/10.1038/srep05729.
Shinar, A.A., Harris, W.H., 1998. Cemented total hip arthroplasty following previous femoral osteotomy. An average 16-year follow up study. J. Arthroplast. 13, 243–253.
Teloken, M.A., Bissett, G., Hozack, W.J., Sharkey, P.F., Rothman, R.H., 2002. Ten to fifteen year follow-up after total hip arthroplasty with a tapered cobalt-chromium femoral component (tri-lock) inserted without cement. J. Bone Jt. Surg. 84-A, 2140–2144.
Veschini, L., Belloni, D., Foglieni, C., Congi, M.G., Ferrarini, M., Caligaris-Cappieand, F., Ferro, E., 2007. Hypoxia-inducible transcription factor-1-alpha determines sensitivity of endothelial cells to the proteosome inhibitor bortezomib. Blood 109 (6), 2565–2570.
Walker, P.S., 1978. Human Joints and Their Artificial Replacement. C.C. Thomas, Springfield.
Wally, Z.J., van Grunsven, W., Claeyssens, F., Goodall, R., Reilly, G.C., 2015. Porous titanium for dental implant applications. Metals 5, 1902–1920.
Wang, W., Ouyang, Y., Poly, C.K., 2011. Orthopaedic implant technology: biomaterials from past to future. Ann. Acad. Med. Singap. 40 (5), 237–244.
Yaszemski, M.J., Trantolo, D.J., Lewendowski, K.V., Hastrei, V., Attobelli, D.E., Wise, D.L. (Eds.), 2003. Biomaterials in Orthopedics. Taylor and Francis Group, London.
Zhao, S., Li, S.J., Hou, W.T., Hao, Y.L., Yang, R., Murr, L.E., 2016. Microstructure and mechanical properties of open cellular Ti-6Al-4V prototypes fabricated by electron beam melting for biomedical applications. Mater. Technol. Adv. Perform. Mater. 31 (2), 98–107.